Journal of Materials Chemistry C

ROYAL SOCIETY OF CHEMISTRY

PAPER

View Article Online
View Journal | View Issue

Cite this: J. Mater. Chem. C, 2023, 11, 3875

Two-dimensional borocarbonitrides for photocatalysis and photovoltaics†

Wei Zhang, *[ab] Changchun Chai,[a] Qingyang Fan,[c] Yintang Yang,[a] Minglei Sun, *[d] Maurizia Palummo[e] and Udo Schwingenschlögl *[d]

Received 10th December 2022,
Accepted 15th February 2023

DOI: 10.1039/d2tc05268g

rsc.li/materials-c

We have designed two-dimensional borocarbonitrides (poly-butadiene-cyclooctatetraene framework BC_2N) with hexagonal unit cells, which are stable according to the cohesive energy, phonon dispersion, *ab initio* molecular dynamics, and elastic modulus results. They are n-type semiconductors with strain-tunable direct band gaps (1.45–2.20 eV), an ultrahigh electron mobility (5.2 × 10^4 cm^2 V^{-1} s^{-1} for β-BC_2N), and strong absorption (an absorption coefficient of up to 10^5 cm^{-1}). The intrinsic electric field due to the Janus geometry of α-BC_2N reduces the recombination of photo-generated carriers. The band edge positions of α-BC_2N and β-BC_2N are suitable for photocatalytic hydrogen production, achieving high solar-to-hydrogen efficiencies of 17% and 12%, respectively, in excess of the typical target value of 10% for industrial application. Both γ-BC_2N and δ-BC_2N can be used as electron donors in type-II heterostructures with two-dimensional transition metal dichalcogenides, and the power conversion efficiency of a solar cell based on these heterostructures can be as high as 21%, approaching the performance of perovskite-based solar cells.

1. Introduction

Increasingly serious environmental pollution, climate abnormalities, and growing energy shortage call for a transition from the current fossil-fuel economy to a low-carbon (or even zero-carbon) economy[1] with a large share of green energy resources such as wind, solar, and hydrogen.[2] Being one of the most promising resources, great scientific efforts have been directed toward the development of environmentally friendly and efficient materials for converting solar energy.[3] Two-dimensional (2D) materials have emerged as outstanding candidates in this endeavor.[4,5]

Photocatalytic water splitting aims at the production of hydrogen and oxygen. The solar-to-hydrogen (STH) efficiency of a photocatalyst is determined jointly from the efficiency of light harvesting and separation of the photogenerated carriers. For many photocatalysts the STH efficiency falls short of the aspired 10%[6] due to low absorbance and carrier recombination. 2D materials, on the other hand, can provide strong absorption of solar radiation and can generate high electrical currents beyond the reach of bulk materials.[7] In addition, their atomic thickness is suitable for photocatalysis, because the distance that the photo-generated carriers have to overcome to participate in chemical reactions (on the surface) is much shorter than in bulk materials. Due to efficient light harvesting and carrier utilization, high STH efficiencies are reported for 2D materials, for example, 10.0% and 6.7% for the ferroelectric and paraelectric phases of $AgBiP_2Se_6$, respectively.[8] The 2D Janus materials B_2P_6, $Pd_4S_3Se_3$, $Pd_4S_3Te_3$, and $Pd_4Se_3Te_3$ even achieve STH efficiencies of 28.2–38.6%.[9,10]

Conversion of solar to electrical energy is another efficient technology for solar energy harvesting. The power conversion efficiency (PCE) achieved by state-of-the-art silicon solar cells is as high as ∼30% and that of perovskite solar cells is as high as ∼26%.[11] Excitonic thin-film solar cells based on 2D van der Waals heterostructures hold the promise of high efficiency due to high carrier mobility and strong absorption of visible light.[12,13] Examples include MoS_2/p-Si (PCE = 5.23%),[14] graphene/GaAs (PCE = 18.5%),[15] and CdS/GeSe (PCE = 1.48%)[16] solar cells. Theoretical studies show PCEs as high as 20.1% in δ-CS/$MoTe_2$[17] and 20% in 2D fullerene/CBN[18] solar cells.

Borocarbonitrides, recently added members of the family of 2D materials, are of interest for application in a variety of

[a] School of Microelectronics, Xidian University, Xi'an 710071, China. E-mail: wzhang-1993@stu.xidian.edu.cn
[b] Beijing Institute of Astronautical Systems Engineering, Beijing 100076, China
[c] College of Information and Control Engineering, Xi'an University of Architecture and Technology, Xi'an 710055, China
[d] Physical Science and Engineering Division (PSE), King Abdullah University of Science and Technology (KAUST), Thuwal 23955-6900, Saudi Arabia. E-mail: minglei.sun@kaust.edu.sa, udo.schwingenschlogl@kaust.edu.sa
[e] Dipartimento di Fisica and INFN, Università di Roma "Tor Vergata", Via della Ricerca Scientifica 1, 00133 Roma, Italy

† Electronic supplementary information (ESI) available: Elastic energies under uniaxial and biaxial strain, phonon spectra under extreme biaxial tensile strain, electronic band structures under biaxial tensile strain, and electronic band structures of 2D transition metal dichalcogenides. POSCAR files. See DOI: https://doi.org/10.1039/d2tc05268g

cutting-edge technologies due to appealing sizes of the provided band gaps.[19–21] Based on the first-principles calculations, we therefore designed new 2D borocarbonitrides, namely, polybutadiene-cyclooctatetraene framework BC_2N (PBCF-BC_2N), employing elemental mutation of poly-butadiene-cyclooctatetraene framework-graphene (PBCF-graphene)[22] and then systematically investigated their stability, electronic structure, and optical properties. Excellent stability is inferred from the obtained cohesive energies, phonon dispersions, and elastic moduli as well as from *ab initio* molecular dynamics simulations. The materials are found to be direct band gap semiconductors with band edge positions suitable for photocatalytic water splitting. We also study the application potential of heterostructures formed from PBCF-BC_2N and transition metal dichalcogenides.

2. Methods

First-principles calculations are performed using the plane-wave Vienna *ab initio* simulation package with projector-augmented wave pseudopotentials.[23] The Perdew–Burke–Ernzerhof (PBE) functional is used for both the structure optimization and calculation of the material properties. The Heyd–Scuseria–Ernzerhof (HSE06) functional with a mixing parameter of 0.25 and a screening parameter of 0.2 $Å^{-1}$ for the Hartree–Fock exchange is adopted to rectify the band gap sizes and band edge positions, because both GW[24] and self-interaction-corrected[25] calculations are computationally much too expensive. The optical absorption spectrum is calculated by means of the random phase approximation method. The plane-wave cutoff energy is set to 500 eV and $9 \times 9 \times 1$ Monkhorst–Pack meshes are utilized for Brillouin zone integrations. Vacuum slabs of 25 Å thickness are applied to generate 2D models. A total energy convergence of 1×10^{-8} eV per atom and an atomic force convergence of 0.001 eV $Å^{-1}$ are achieved. The phonon spectra are calculated using density functional perturbation theory (Phonopy[26] and Vienna *ab initio* simulation package) and a $3 \times 3 \times 1$ supercell. *Ab initio* molecular dynamics simulations at 1000 K are carried out for 10 ps (time step 1 fs) using a $3 \times 3 \times 1$ supercell and a canonical ensemble.[27]

3. Results and discussion

3.1 Structure and stability

Starting from the structure of PBCF-graphene,[22] we design four ternary structures of PBCF-BC_2N by replacing half of the C–C pairs with B–N pairs, see the optimized structures in Fig. 1 and structural details in Table 1. In each case, the primitive hexagonal unit cell contains six B, twelve C, and six N atoms. It turns out that α-BC_2N, β-BC_2N, γ-BC_2N, and δ-BC_2N have space groups *P6mm* (no. 183), $P\bar{3}m1$ (no. 164), $P\bar{6}_2m$ (no. 189), and $P\bar{3}_1m$ (no. 162), respectively, with optimized lattice constants of 6.99, 7.05, 7.14, and 7.13 Å. The orthorhombic lattice constants are 6.99 Å (armchair direction) and 12.11 Å (zigzag direction) for α-BC_2N, 7.05 Å and 12.21 Å for β-BC_2N, 7.14 Å and 12.37 Å for γ-BC_2N, and 7.13 Å and 12.35 Å for δ-BC_2N. The sandwich-like structures are 2.47 to 2.53 Å thick. The top and bottom layers of α-BC_2N and β-BC_2N are connected by B–N bonds while those of γ-BC_2N and δ-BC_2N are connected by C=C bonds. α-BC_2N realizes a pronounced Janus geometry. In each case, the hexagonal unit cell comprises six C–C, six B–N, twelve C–B, and twelve C–N bonds. The C=C bond lengths of 1.36 to 1.39 Å are slightly shorter than those in graphene (1.42 Å), whereas the B–N bond lengths of 1.44 to 1.46 Å closely resemble the value for h-BN (1.45 Å). The relatively short C=C and B–N bond lengths represent strong covalent bonds. The C–B and C–N bond lengths range from 1.53 to 1.60 Å and from 1.45 to 1.48 Å, respectively.

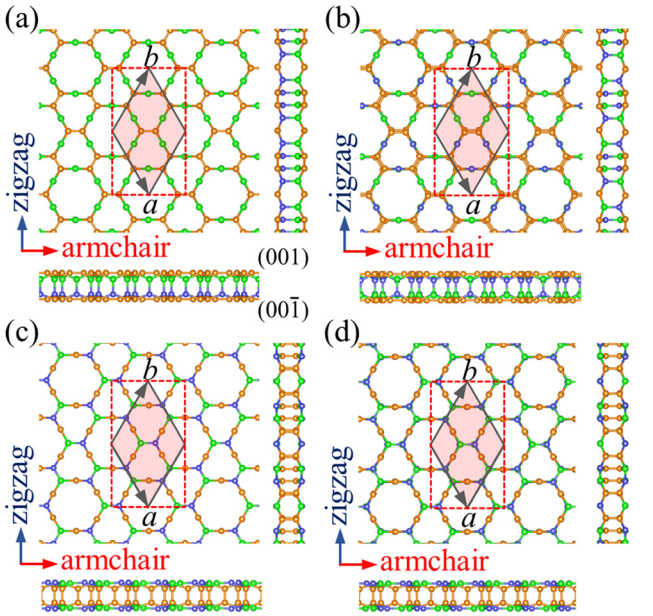

Fig. 1 Top and side views of the atomic structures of (a) α-BC_2N, (b) β-BC_2N, (c) γ-BC_2N, and (d) δ-BC_2N. The primitive hexagonal unit cell is shown by gray solid lines and the orthorhombic unit cell is shown by red dashed lines. The orange, green, and blue spheres represent C, B, and N atoms, respectively.

Table 1 Space groups, lattice constants (*a*), thickness (*h*), bond lengths (l_{C-N}, l_{C-B}, and l_{B-N}), cohesive energy (E_{coh}), and band gaps (E_g^{PBE} and E_g^{HSE06})

	Space group	*a* (Å)	*h* (Å)	l_{C-C} (Å)	l_{C-N} (Å)	l_{C-B} (Å)	l_{B-N} (Å)	E_{coh} (eV per atom)	E_g^{PBE} (eV)	E_g^{HSE06} (eV)
α-BC_2N	*P6mm*	6.99	2.53	1.36/1.39	1.48	1.53	1.46	6.25	0.75	1.97
β-BC_2N	$P\bar{3}m1$	7.05	2.51	1.37	1.45	1.59	1.44	6.31	1.10	2.20
γ-BC_2N	$P\bar{6}_2m$	7.14	2.53	1.36	1.46	1.60	1.44	6.33	0.46	1.45
δ-BC_2N	$P\bar{3}_1m$	7.13	2.47	1.36	1.46	1.59	1.44	6.31	0.66	1.68

To analyze the chemical bonding in PBCF-BC_2N, we calculate the electron localization function, as plotted in Fig. 2. Localized electrons between the atoms represent covalent C=C, B–N, C–B, and C–N bonds. The obtained Bader charges agree with the electronegativities of the involved atoms: for α-BC_2N the C and B atoms on the (001) side show values of +1.29 and −1.96 *e*, respectively, while the C and N atoms on the (00$\bar{1}$) side show values of −0.64 and +1.31 *e*. For β-BC_2N, γ-BC_2N, and δ-BC_2N,

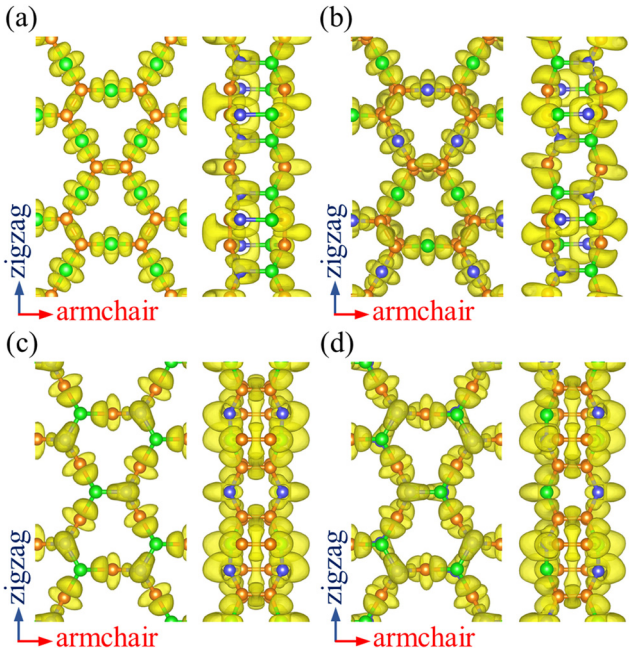

Fig. 2 Electron localization function (isosurface value 0.8) of (a) α-BC_2N, (b) β-BC_2N, (c) γ-BC_2N, and (d) δ-BC_2N.

respectively, we obtain Bader charges of −1.90, −1.94, and −1.96 *e* for the B atoms, +0.25, +0.28, and +0.28 e for the C atoms, and +1.40, +1.38, and +1.40 *e* for the N atoms. Hence, the chemical bonding in PBCF-BC_2N is governed by strongly polarized covalent bonds.

The cohesive energy per atom, $E_{coh} = [xE(B) + yE(C) + zE(N) - xE(B_xC_yN_z)]/(x + y + z)$, where $E(B)$, $E(C)$, $E(N)$, and $E(B_xC_yN_z)$ are the total energies of a B atom, a C atom, a N atom, and a unit cell of PBCF-BC_2N, respectively, follows the trend γ-BC_2N (6.33 eV) > β-BC_2N (6.31 eV) = δ-BC_2N (6.31 eV) > α-BC_2N (6.25 eV). It is lower than in the cases of graphene (7.85 eV) and h-BN (7.07 eV) but higher than in the cases of (experimentally existing) *N*-graphdiyne (6.02 eV),[28] *B*-graphdiyne (5.85 eV),[29] and g-C_3N_4 (5.71 eV),[30] demonstrating pronounced stability. The obtained phonon spectra and densities of states in Fig. 3 demonstrate dynamical stability. The maximal phonon frequencies turn out to be 46.6, 44.4, 45.2, and 44.9 THz for α-BC_2N, β-BC_2N, γ-BC_2N, and δ-BC_2N, respectively. The high-frequency phonons are due to the presence of sp^2-hybridized C atoms, whereas the B and N atoms contribute below 40 THz. Our *ab initio* molecular dynamics simulations, see Fig. 3 for the potential energy as a function of the time and the final atomic structure, demonstrate the absence of bond breaking.

The mechanical properties of PBCF-BC_2N are investigated by calculating the in-plane elastic constants, Young's modulus, Poisson's ratio, and the strain–stress relationship. The hexagonal lattice results in isotropic in-plane elasticity and the elastic energy accumulated under strain ε_{ij} can be expressed as

$$U = \frac{1}{2}C_{11}\left(\varepsilon_{xx}^2 + \varepsilon_{yy}^2 + 2\varepsilon_{xy}^2\right) + C_{12}\left(\varepsilon_{xx}\varepsilon_{yy} - \varepsilon_{xy}^2\right). \quad (1)$$

Perfect parabolic dependencies under uniaxial and biaxial strain (Fig. S1, ESI†) demonstrate reliability of the employed calculation method. Fulfilling the relations $C_{11} = C_{22}$ and

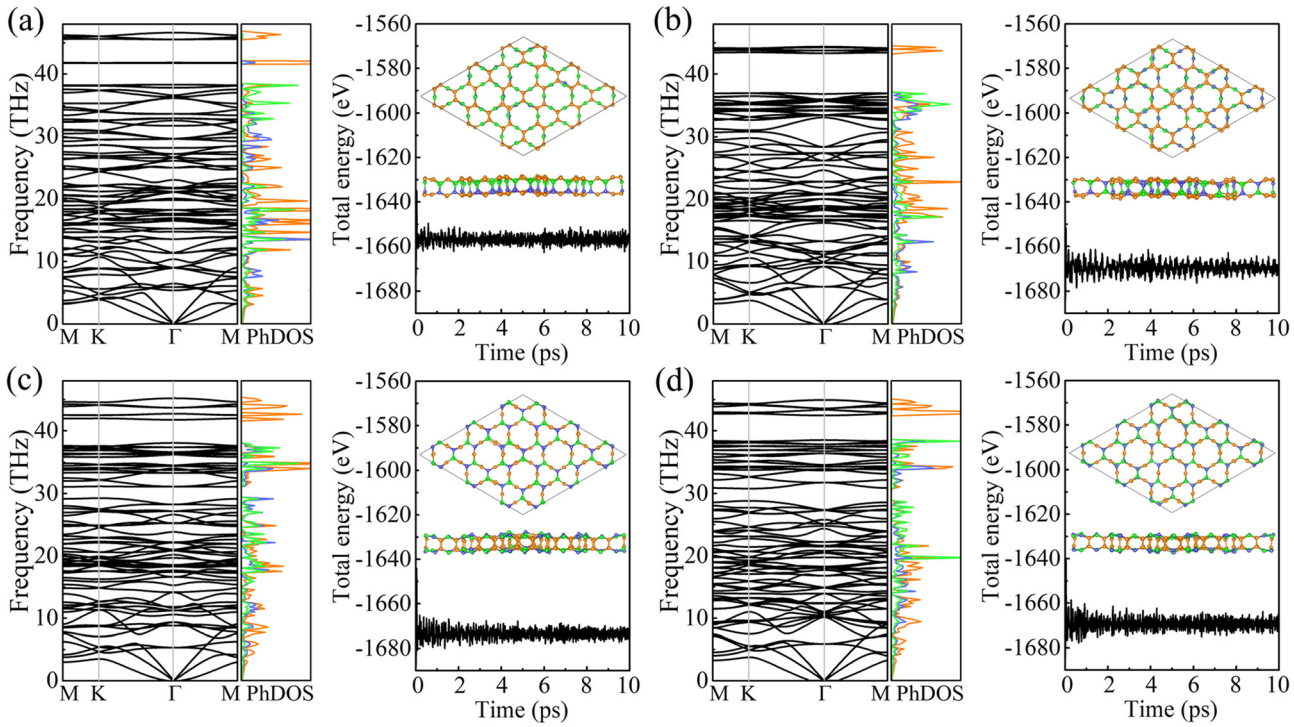

Fig. 3 Phonon spectra and densities of states (left; colors correspond to the atomic species) as well as results of *ab initio* molecular dynamics simulations (right; at 1000 K) of (a) α-BC_2N, (b) β-BC_2N, (c) γ-BC_2N, and (d) δ-BC_2N.

$2C_{44} = C_{11} - C_{12}$ we obtain the elastic constant C_{11}, C_{12}, and C_{44} values of 236, 100, and 68 N m^{-1} for α-BC_2N; 230, 84, and 73 N m^{-1} for β-BC_2N; 237, 73, and 82 N m^{-1} for γ-BC_2N; and 223, 62 and 80 N m^{-1} for δ-BC_2N, respectively. Therefore, the Born criteria ($C_{44} > 0$ and $C_{11}C_{22} - C_{12}^2 > 0$)[31] of mechanical stability are satisfied. The in-plane Young's modulus $Y = (C_{11}^2 - C_{12}^2)/C_{11}$ and Poisson's ratio $\nu = C_{12}/C_{11}$ amount to 194 N m^{-1} and 0.42 for α-BC_2N; 199 N m^{-1} and 0.37 for β-BC_2N; 215 N m^{-1} and 0.31 for γ-BC_2N; and 206 N m^{-1} and 0.28 for δ-BC_2N. The Young's modulus is thus lower than that in graphene (344 N m^{-1})[32] but much higher than those in MoS_2 (123 N m^{-1})[33] and black phosphorene (83 N m^{-1}),[34] indicating mechanical robustness.

Strain–stress curves under biaxial strain are shown in Fig. 4(a). When the strain increases, the stress is found to increase first linearly and afterwards nonlinearly. The fracture strength and strain turn out to be 23.6 N m^{-1} and 16% for α-BC_2N; 18.7 N m^{-1} and 18.5% for β-BC_2N; 18.1 N m^{-1} and 16.5% for γ-BC_2N; and 15.6 N m^{-1} and 13% for δ-BC_2N. In contrast to α-BC_2N, β-BC_2N, and γ-BC_2N, we find for δ-BC_2N, a sudden drop in stress under high strain (between 13.5% and 14%). Comparison of the electron localization functions of δ-BC_2N under 13.5% and 14% strain in Fig. 4(b) and (c) points to the strengthening of the inter-layer B–N bonds at the cost of intra-layer bonds, resulting in structural collapse. The calculated phonon spectra of α-BC_2N, β-BC_2N, γ-BC_2N, and δ-BC_2N (Fig. S2, ESI†), on the other hand, show no imaginary frequencies under 8%, 18%, 16%, and 12% strain, respectively (while showing imaginary frequencies under 8.5%, 18.5%, 16.5%, and 12.5% strain), which correspond to fracture strengths of 18.3 N m^{-1}, 18.7 N m^{-1}, 18.1 N m^{-1}, and 15.5 N m^{-1}, respectively.

3.2 Electronic properties

Fig. 5 shows the electronic band structures and partial densities of states of PBCF-BC_2N obtained using the PBE and HSE06 functionals. In each case we find a direct band gap with the conduction band minimum (CBM) and valence band maximum (VBM) located at the center of the Brillouin zone (Γ point). The size of the band gap of α-BC_2N, β-BC_2N, γ-BC_2N, and δ-BC_2N is found to be 1.97 (0.84), 2.20 (1.13), 1.45 (0.54), and 1.68 (0.70) eV using the PBE (HSE06) functional, respectively. The CBM of α-BC_2N (β-BC_2N) is dominated by the C (B) atoms and the VBM is dominated by the B (N) and C atoms. The CBM of both γ-BC_2N and δ-BC_2N is dominated by B atoms (with contributions of the N atoms) and the VBM by the C atoms.

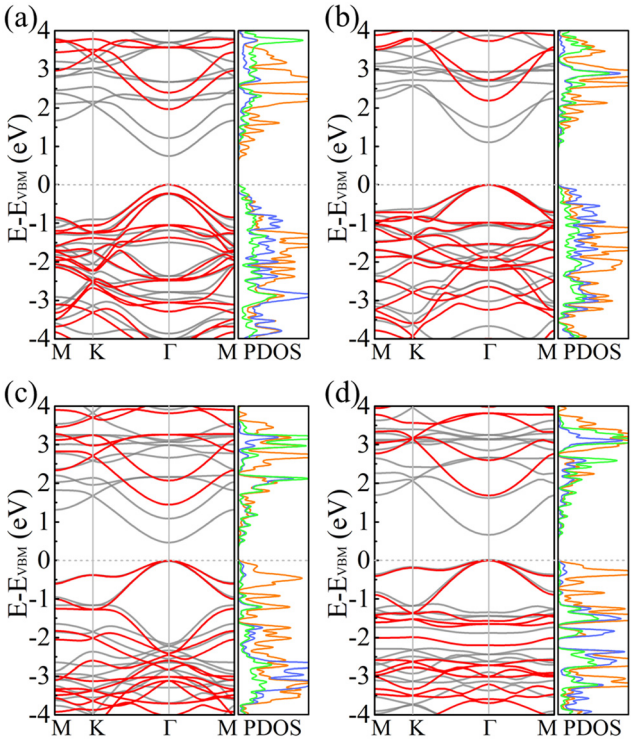

Fig. 5 Electronic band structures (black = PBE and red = HSE06) and partial densities of states (PBE; in units of 1/eV; orange = C; green = B; blue = N) of (a) α-BC_2N, (b) β-BC_2N, (c) γ-BC_2N, and (d) δ-BC_2N.

For the HSE06 functional, the effect of biaxial strain on the size of the band gap is shown in Fig. 6(a) (see Fig. S3, ESI† for the electronic band structures). With the exception of α-BC_2N, the strain tunes the size of the band gap effectively. For the PBE functional, the carrier effective mass is obtained by fitting the electronic band structure at the respective band edge as $m^* = \hbar^2/(\partial^2 E/\partial k^2)^{-1}$; see the results in Fig. 6(b) and (c). The electron (hole) effective masses of PBCF-BC_2N turn out to be isotropic with values of 0.37 (0.49), 0.44 (0.80), 0.47 (0.77), and 0.60 (1.04) m_0 for α-BC_2N, β-BC_2N, γ-BC_2N, and δ-BC_2N in the absence of

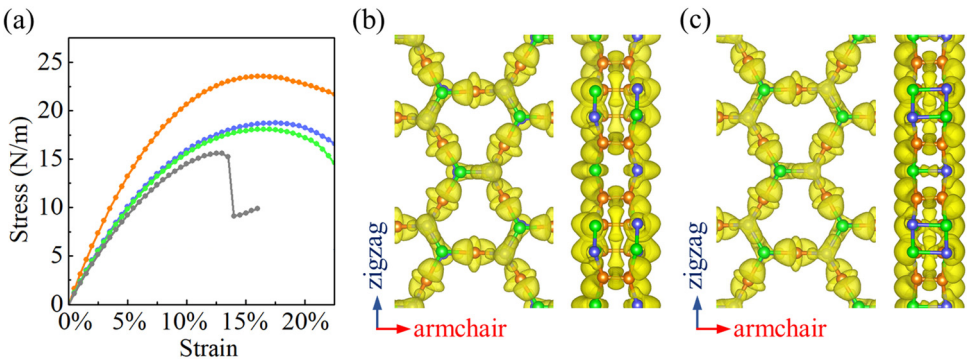

Fig. 4 (a) Strain–stress curves under biaxial strain (orange = α-BC_2N; blue = β-BC_2N, green = γ-BC_2N, and gray = δ-BC_2N). Electron localization function (isosurface value = 0.8) of δ-BC_2N under (b) 13.5% and (c) 14% biaxial strain.

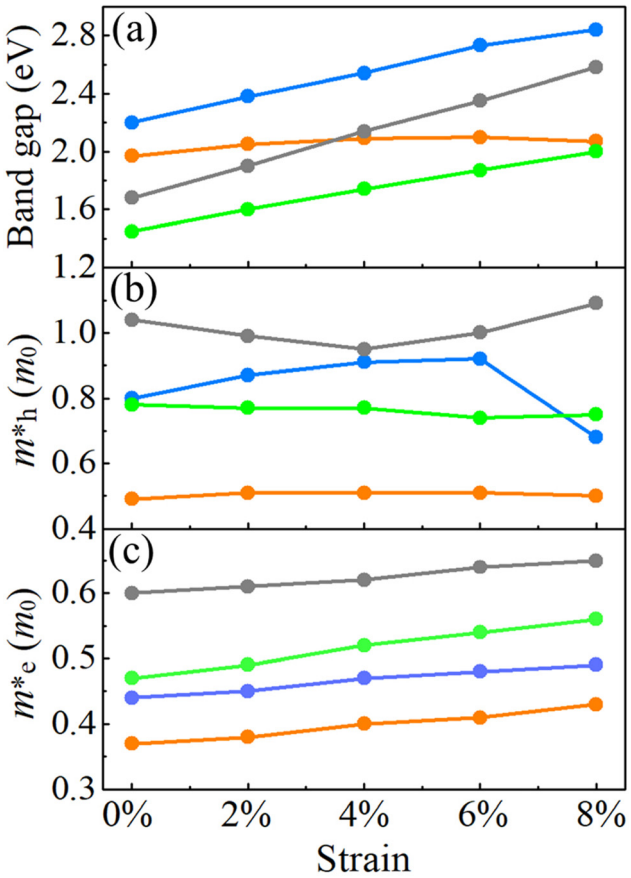

Fig. 6 (a) Band gaps, (b) hole effective masses and (c) electron effective masses of PBCF-BC_2N under biaxial strain (orange = α-BC_2N; blue = β-BC_2N, green = γ-BC_2N, and gray = δ-BC_2N).

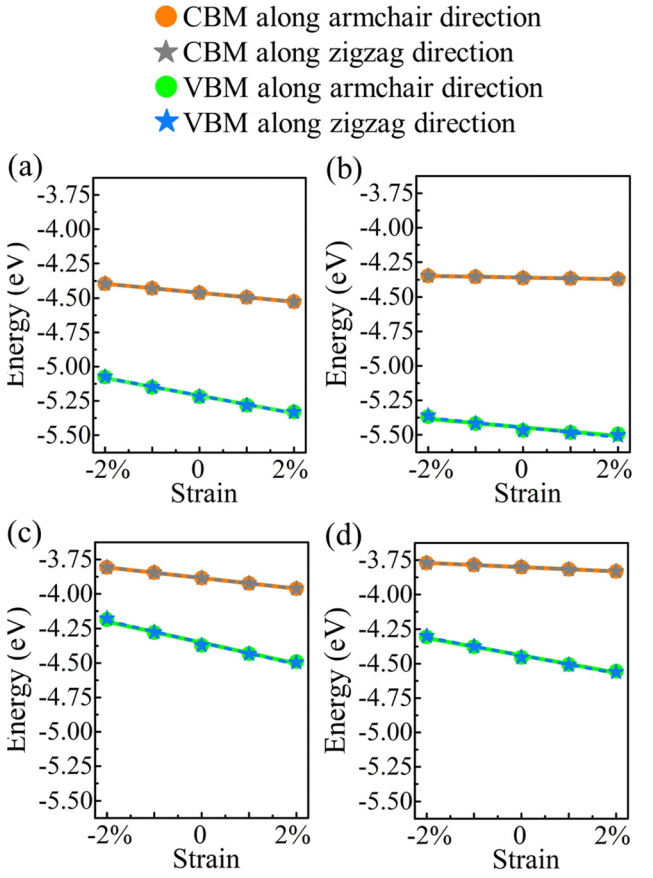

Fig. 7 Valence and conduction band edges of (a) α-BC_2N, (b) β-BC_2N, (c) γ-BC_2N, and (d) δ-BC_2N under biaxial strain.

strain, respectively. The electron effective masses increase slowly under strain, while the hole effective masses show a more complex behavior.

The carrier mobility is calculated using the Bardeen–Shockley deformation potential theory as

$$\mu_d = \frac{e\hbar^3 C_{2D}}{k_B T (m^*)^2 E^2}, \quad (2)$$

where C_{2D} denotes the in-plane elastic constant and E denotes the (direction-dependent) deformation potential constant. The results should be understood as upper limits, since the carrier mobility tends to be overestimated. The band edge positions under strain along the armchair and zigzag directions are shown in Fig. 7. Table 2 summarizes the obtained in-plane elastic constants, deformation potential constants, and carrier mobilities at 300 K. We find virtually no anisotropy for electron mobilities and only a minor anisotropy for hole mobilities. All the materials show significantly larger electron mobilities than hole mobilities, where the particularly high electron mobility of β-BC_2N is a consequence of a small deformational potential constant. The hole mobilities of α-BC_2N and β-BC_2N exceed those of 2D MoS_2 (armchair direction: 2.0×10^2 cm^2 V^{-1} s^{-1} and zigzag direction: 1.5×10^2 cm^2 V^{-1} s^{-1})[35] by more than a factor of two and all the electron mobilities exceed those of 2D MoS_2 (armchair direction: 7.2×10^1 cm^2 V^{-1} s^{-1} and zigzag direction: 6.2×10^1 cm^2 V^{-1} s^{-1} in the)[36] by about two orders of magnitude, resembling few-layer black phosphorus.[36] The electron mobility of β-BC_2N is even comparable to that of 2D $Ca_3Sn_2S_7$ (6.7×10^4 cm^2 V^{-1} s^{-1}),[37] suggesting its great potential for application in nano-electronic devices.

3.3 Photocatalytic properties

To investigate the photocatalytic potential for water splitting, we determined the positions of the band edges with respect to

Table 2 Carrier effective mass (m^*), in-plane elastic constants (C^{2D}), deformation potential constants ($E_{armchair}$ and E_{zigzag}), and carrier mobilities at 300 K ($\mu_{armchair}$ and μ_{zigzag})

	Carrier type	m^* (m_0)	C^{2D} (N m^{-1})	$E_{armchair}$ (eV)	E_{zigzag} (eV)	$\mu_{armchair}$ (cm^2 V^{-1} s^{-1})	μ_{zigzag} (cm^2 V^{-1} s^{-1})
α-BC_2N	Electron	0.37	236	3.28	3.29	4.8×10^3	4.8×10^3
β-BC_2N		0.44	230	0.82	0.83	5.2×10^4	5.2×10^4
γ-BC_2N		0.47	237	3.86	3.86	2.1×10^3	2.1×10^3
δ-BC_2N		0.60	223	1.54	1.54	7.8×10^3	7.8×10^3
α-BC_2N	Hole	0.49	236	6.39	6.51	7.2×10^2	6.9×10^2
β-BC_2N		0.80	230	5.02	5.21	4.2×10^2	3.9×10^2
γ-BC_2N		0.78	237	7.62	7.93	2.1×10^2	1.9×10^2
δ-BC_2N		1.04	223	6.28	6.57	1.5×10^2	1.4×10^2

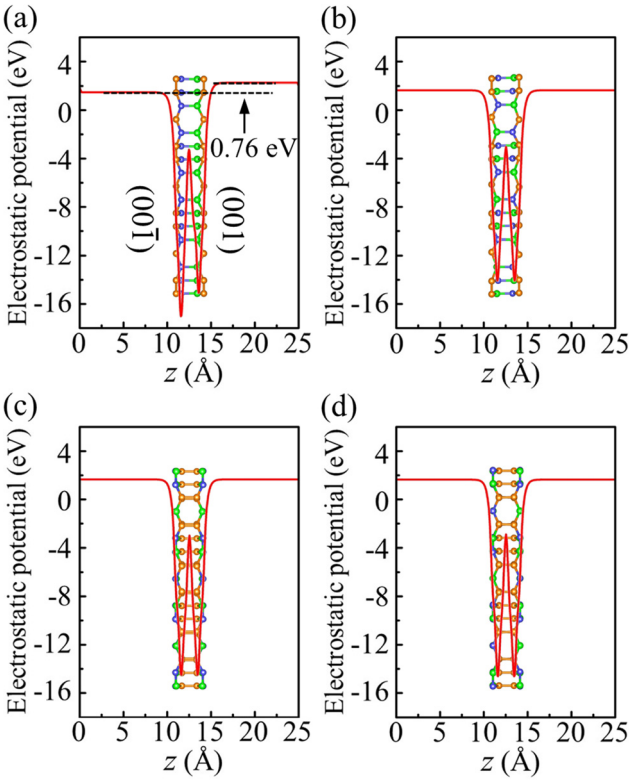

Fig. 8 Electrostatic potential of (a) α-BC_2N, (b) β-BC_2N, (c) γ-BC_2N, and (d) δ-BC_2N.

the vacuum level using the HSE06 functional. One of the fundamental requirements of a photocatalytic semiconductor is band edges (CBM and VBM) enclosing the redox potentials of water, *i.e.*, the CBM must exceed the reduction potential of H^+/H_2 (−4.44 eV at pH = 0 and −4.03 eV at pH = 7) and the VBM must not exceed the oxidation potential of O_2/H_2O (−5.67 eV at pH = 0 and −5.26 eV at pH = 7).[38] To determine the positions of the band edges, we have shown the electrostatic potential in Fig. 8. Due to its Janus geometry, the value is different for the two sides of α-BC_2N (specifically: 0.76 eV higher for the (001) side than the (00$\bar{1}$) side).

Strain engineering is an effective approach to modulate the electronic properties of materials,[39–41] and the effect of strain on the positions of the band edges is shown in Fig. 9(a)–(e). For α-BC_2N we find that the (001) side is suitable only for the oxygen evolution reaction and the (00$\bar{1}$) side is suitable only for the hydrogen evolution reaction, see Fig. 9(f). Photocatalytic water splitting is possible for β-BC_2N (from pH = 0 to pH = 7), while for γ-BC_2N and δ-BC_2N it is possible only under at least 6% strain. Strong optical absorption from the visible to ultraviolet spectral range is another key requirement of a high-efficiency photocatalytic semiconductor. The optical spectra in Fig. 10, calculated by random approximation (RPA) with the polarization being parallel to the 2D material, show that PBCF-BC_2N fulfills this requirement even though the RPA does not include excitonic effects[42,43] (renormalization of the peak intensities, redshifting of the spectra due to electron–hole interaction, *etc.*) and these effects can be significant in 2D materials.

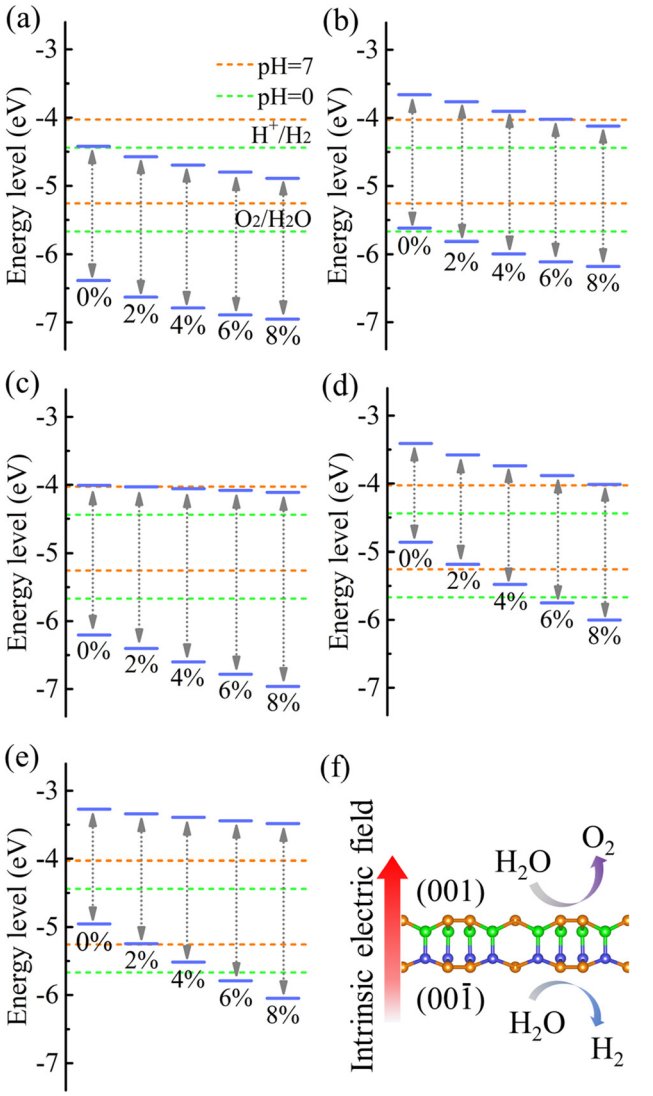

Fig. 9 Positions of the band edges relative to the vacuum level of (a) (001) side of α-BC_2N, (b) (00$\bar{1}$) side of α-BC_2N, (c) β-BC_2N, (d) γ-BC_2N, and (e) δ-BC_2N under biaxial strain. (f) Intrinsic electric field of α-BC_2N.

We next quantify the photocatalytic performance. The STH efficiency is estimated from $\eta_{sth} = \eta_{ab} \times \eta_{cu}$, where η_{ab} is the efficiency of absorption and η_{cu} is the efficiency of carrier utilization. We have

$$\eta_{ab} = \frac{\int_{E_g}^{\infty} P(\hbar\omega)\mathrm{d}(\hbar\omega)}{\int_{0}^{\infty} P(\hbar\omega)\mathrm{d}(\hbar\omega)}, \quad (3)$$

where E_g is the optical gap (1.97 eV for α-BC_2N and 2.20 eV for β-BC_2N) and $P(\hbar\omega)$ is the AM1.5 solar energy flux at photon energy $\hbar\omega$, resulting in η_{ab} = 37.7% for α-BC_2N and 28.2% for β-BC_2N. Furthermore, we have

$$\eta_{cu} = \frac{\Delta G \int_{E_{min}}^{\infty} \frac{P(\hbar\omega)}{\hbar\omega}\mathrm{d}(\hbar\omega)}{\int_{E_g}^{\infty} P(\hbar\omega)\mathrm{d}(\hbar\omega)}, \quad (4)$$

where ΔG = 1.23 eV for water and E_{min} (minimum energy of the photons that can be utilized for the redox reactions) can be

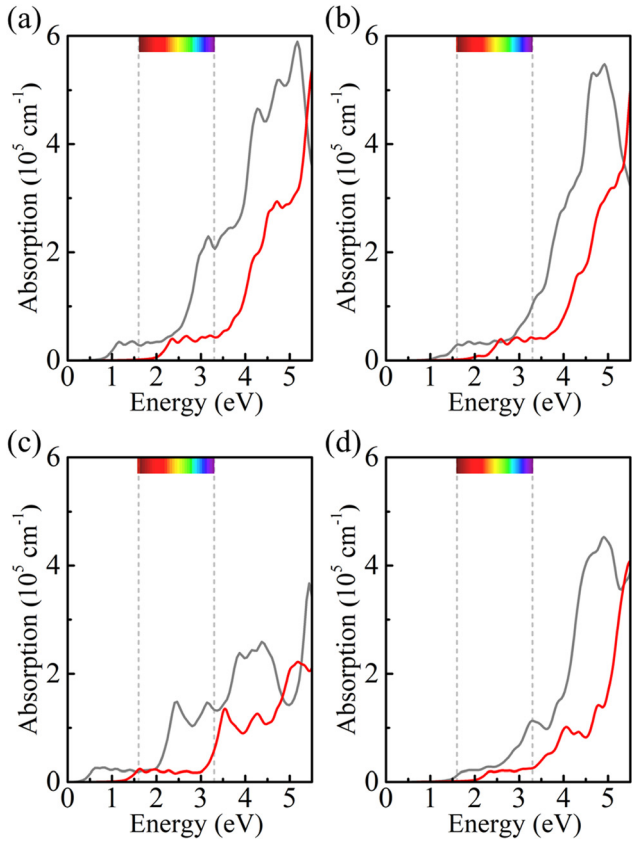

Fig. 10 Optical spectra of (a) α-BC_2N, (b) β-BC_2N, (c) γ-BC_2N, and (d) δ-BC_2N (gray = PBE + RPA; red = HSE06 + RPA; polarization parallel to the 2D material).

determined as

$$E_{\min} = \begin{cases} E_g & (\chi(H_2) \geq 0.2, \chi(O_2) \geq 0.6), \\ E_g + 0.2 - \chi(H_2) & (\chi(H_2) < 0.2, \chi(O_2) \geq 0.6), \\ E_g + 0.6 - \chi(O_2) & (\chi(H_2) \geq 0.2, \chi(O_2) < 0.6), \\ E_g + 0.8 - \chi(H_2) - \chi(O_2) & (\chi(H_2) < 0.2, \chi(O_2) < 0.6), \end{cases} \quad (5)$$

where $\chi(H_2)$ and $\chi(O_2)$ represent the overpotentials of the hydrogen and oxygen evolution reactions, respectively. Considering that the intrinsic electric field of a Janus material reduces the recombination of the photo-generated carriers, the STH efficiency is corrected as

$$\eta'_{STH} = \eta_{STH} \times \frac{\int_0^\infty P(\hbar\omega)\mathrm{d}(\hbar\omega)}{\int_0^\infty P(\hbar\omega)\mathrm{d}(\hbar\omega) + \Delta\Phi\int_{E_g}^\infty \frac{P(\hbar\omega)}{\hbar\omega}\mathrm{d}(\hbar\omega)}, \quad (6)$$

where $\Delta\Phi$ is the electrostatic potential difference between the two sides of the materials. We find $\chi(H_2)$ = 0.78 eV, $\chi(O_2)$ = 0.72 eV, E_{min} = 1.97 eV, $\Delta\Phi$ = 0.76 eV, and η_{cu} = 49.4% for α-BC_2N and $\chi(H_2)$ = 0.43 eV, $\chi(O_2)$ = 0.53 eV, E_{min} = 2.27 eV, and η_{cu} = 40.8% for β-BC_2N. Thus, the STH efficiency and corrected STH efficiency of α-BC_2N turn out to be 19% and 17%, respectively, approaching the conventional theoretical limit (~18%). The STH efficiency of β-BC_2N turns out to be 12%, which is comparable to the values reported for GeN_3 (12.6%)[44] and $AgBiP_2Se_6$ (10.2%),[26] exceeding the target value for industrial application (10%).[19] Both α-BC_2N and β-BC_2N therefore emerge as economically viable photocatalysts for water splitting.

3.4 Photovoltaic properties

Due to their moderate direct band gaps of 1.45 and 1.68 eV, respectively, and excellent absorption of solar radiation, γ-BC_2N and δ-BC_2N are potential candidates for heterostructure solar cell materials. We study heterostructures with hexagonal 2D MX_2 (M = Mo and W; X = S, Se, and Te), which also show direct band gaps and strong absorption.[45–47] Table 3 summarizes the structural and electronic parameters of 2D MX_2 (M = Mo and W; X = S, Se, and Te) obtained using the HSE06 hybrid functional with spin–orbital coupling (SOC) being included (see Fig. S4, ESI† for the electronic band structures). The positions of the valence and conduction band edges relative to the vacuum level are illustrated in Fig. 11(a). The band edges of γ-BC_2N and δ-BC_2N enclose those of WTe_2, leading to type-I band alignment, while they are interlaced with those of MoS_2, $MoSe_2$, $MoTe_2$, WS_2, and WSe_2, leading to type-II band alignment. Due to the lower electron affinity as compared to 2D MX_2 (M = Mo and W; X = S, Se, and Te), both γ-BC_2N and δ-BC_2N act as electron donors in the heterostructure. For γ-BC_2N (δ-BC_2N), we obtain conduction band offsets of 0.84 (0.98), 0.48 (0.62), 0.31 (0.45), 0.43 (0.57), 0.12 (0.26), and 0.14 (0.28) eV relative to MoS_2, $MoSe_2$, $MoTe_2$, WS_2, WSe_2, and WTe_2, respectively.

The maximum PCE of a solar cell is given using the following expression

$$PCE_{max} = \frac{\beta_{FF} V_{OC} J_{SC}}{\int_0^\infty P(\hbar\omega)\mathrm{d}(\hbar\omega)}, \quad (7)$$

where we assume a fill factor of β_{FF} = 0.65. The open circuit voltage

$$V_{OC} = \frac{1}{e}\left(E_g^d - \Delta E_{CBM} - 0.3\right) \quad (8)$$

can be obtained from the optical gap of the donor ($E_g^d \sim$ 1.45 eV for γ-BC_2N and 1.68 eV for δ-BC_2N) and conduction band offset (ΔE_{CBM}) considering an empirical loss of 0.3 eV. The short circuit current (limit of external quantum efficiency) is given using the

Table 3 Lattice constants (*a*; space group $P\bar{6}m2$), thickness (*h*), bond lengths (l_{M-X}), positions of the band edges with respect to the vacuum level ($E_{VBM}^{HSE06+SOC}$ and $E_{CBM}^{HSE06+SOC}$), band gaps ($E_g^{HSE06+SOC}$), and spin–orbit splitting in the valence band ($\Delta^{HSE06+SOC}$)

	a (Å)	*h* (Å)	l_{M-X} (Å)	$E_{VBM}^{HSE06+SOC}$ (eV)	$E_{CBM}^{HSE06+SOC}$ (eV)	$E_g^{HSE06+SOC}$ (eV)	$\Delta^{HSE06+SOC}$ (eV)
MoS_2	3.18	3.13	2.41	−6.27	−4.25	2.02	0.21
$MoSe_2$	3.32	3.34	2.54	−5.60	−3.89	1.71	0.28
$MoTe_2$	3.55	3.61	2.73	−4.99	−3.72	1.27	0.35
WS_2	3.18	3.14	2.42	−5.83	−3.84	1.99	0.55
WSe_2	3.32	3.35	2.55	−5.17	−3.53	1.64	0.62
WTe_2	3.55	3.62	2.74	−4.59	−3.55	1.04	0.68

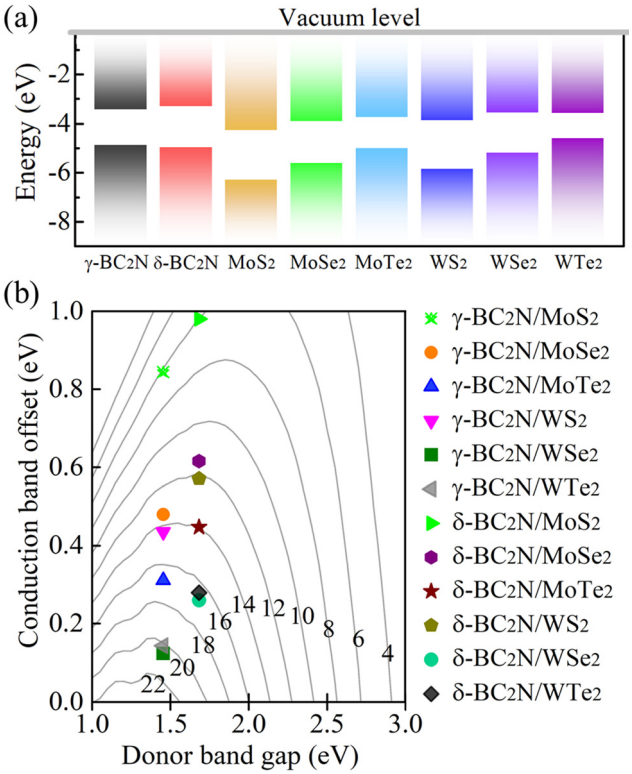

Fig. 11 (a) Band alignments and (b) PCE (in %).

following expression

$$J_{SC} = e\int_{E_g^d}^{\infty} \frac{P(\hbar\omega)}{\hbar\omega} d(\hbar\omega). \quad (9)$$

As shown in Fig. 11(b), PCE_{max} values in excess of 20% are achieved by the γ-BC_2N/WSe_2 and γ-BC_2N/WTe_2 heterostructures, which are comparable to those of organic solar cells (18.2%)[11] and the δ-CS/$MoTe_2$ heterostructure (20.1%).[17] They approach the performances of state-of-the-art perovskites (25.5%), silicon (27.6%), and GaAs (30.5%) solar cells,[11] pointing toward their great application potential.

4. Conclusion

Using comprehensive first-principles calculations, we have proposed 2D hexagonal borocarbonitrides (α-BC_2N, β-BC_2N, γ-BC_2N, and δ-BC_2N) with cohesive energies of 6.25–6.33 eV per atom combined with dynamical, mechanical, and thermal (at 1000 K) stability. High fracture strengths and strains are interesting for nano-mechanical applications. Moderate direct band gaps of 1.45–2.20 eV (HSE06) and isotropic small carrier effective masses are found. It also turns out that the size of the band gap can be effectively tuned using strain. Electronic applications can benefit from the discovered ultrahigh electron mobilities. Both α-BC_2N and β-BC_2N show potential in photocatalytic water splitting with excellent absorption of solar radiation. In particular, the intrinsic electric field induced by the Janus geometry of α-BC_2N separates the photo-generated electrons and holes, therefore minimizing their recombination. The electrons and holes migrate to opposite sides of the two-dimensional material to take part in the redox reactions for water splitting. The high efficiency of carrier utilization (49.4%) resulting from the intrinsic electric field leads to an outstanding solar-to-hydrogen efficiency of 17%. According to the band alignments, γ-BC_2N and δ-BC_2N act as electron donors in heterostructures with 2D MX_2 (M = Mo and W; X = S, Se, and Te). It turns out that such heterostructures can show a PCE of up to 21%.

Author contributions

W. Zhang, M. Sun, and U. Schwingenschlögl conceived the study. C. Chai and M. Sun performed the calculations and analyzed the data. W. Zhang and Q. Fan wrote the manuscript guided by M. Sun, M. Palummo, and U. Schwingenschlögl. C. Chai and Y. Yang provided equipment support.

Conflicts of interest

The authors declare no competing interests.

Acknowledgements

The authors acknowledge financial support from the National Natural Science Foundation of China (no. 61974116 and no. 61804120), the China Postdoctoral Science Foundation (no. 2019TQ0243 and no. 2019M663646), and the Key Scientific Research Project of Education Department of Shannxi-Key Laboratory Project (no. 20JS066). M. P. acknowledges CN1 (Spoke6) - Centro Nazionale di Ricerca (High-Performance Computing Big Data and Quantum Computing and TIME2-QUEST-INFN projects). Xidian University provided computational resources and support. The research reported in this publication was supported by funding from King Abdullah University of Science and Technology (KAUST).

References

1 S. Carley and D. M. Konisky, The justice and equity implications of the clean energy transition, *Nat. Energy*, 2020, **5**, 569–577.
2 R. Fouquet, Historical energy transitions: Speed, prices and system transformation, *Energy Res. Soc. Sci.*, 2016, **22**, 7–12.
3 F. Creutzig, P. Agoston, J. C. Goldschmidt, G. Luderer, G. Nemet and R. C. Pietzcker, The underestimated potential of solar energy to mitigate climate change, *Nat. Energy*, 2017, **2**, 17140.
4 P. Miró, M. Audiffred and T. Heine, An atlas of two-dimensional materials, *Chem. Soc. Rev.*, 2014, **43**, 6537–6554.
5 M. Buscema, J. O. Island, D. J. Groenendijk, S. I. Blanter, G. A. Steele, H. S. J. van der Zant and A. Castellanos-Gomez, Photocurrent generation with two-dimensional van der Waals semiconductors, *Chem. Soc. Rev.*, 2015, **44**, 3691–3718.

6 C. R. Cox, J. Z. Lee, D. G. Nocera and T. Buonassisi, Ten-percent solar-to-fuel conversion with nonprecious materials, *Proc. Natl. Acad. Sci. U. S. A.*, 2014, **111**, 14057–14061.
7 M. Bernardi, M. Palummo and J. C. Grossman, Extraordinary sunlight absorption and one nanometer thick photovoltaics using two-dimensional monolayer materials, *Nano Lett.*, 2013, **13**, 3664–3670.
8 L. Ju, J. Shang, X. Tang and L. Kou, Tunable photocatalytic water splitting by the ferroelectric switch in a 2D $AgBiP_2Se_6$ monolayer, *J. Am. Chem. Soc.*, 2019, **142**, 1492–1500.
9 M. Sun and U. Schwingenschlögl, B_2P_6: A two-dimensional anisotropic Janus material with potential in potocatalytic water splitting and metal-ion batteries, *Chem. Mater.*, 2020, **32**, 4795–4800.
10 Y. Luo, M. Sun, J. Yu and U. Schwingenschlögl, $Pd_4S_3Se_3$, $Pd_4S_3Te_3$, and $Pd_4Se_3Te_3$: Candidate two-dimensional Janus materials for photocatalytic water splitting, *Chem. Mater.*, 2021, **33**, 4128–4134.
11 M. A. Green, E. D. Dunlop, J. Hohl-Ebinger, M. Yoshita, N. Kopidakis and X. Hao, Applications, Solar cell efficiency tables (Version 58), *Prog. Phot. Res. Appl.*, 2021, **29**, 657–667.
12 M. Bernardi, M. Palummo and J. C. Grossman, Semiconducting monolayer materials as a tunable platform for excitonic solar cells, *ACS Nano*, 2012, **6**, 10082–10089.
13 M. M. Furchi, A. Pospischil, F. Libisch, J. Burgdörfer and T. Mueller, Photovoltaic effect in an electrically tunable van der Waals heterojunction, *Nano Lett.*, 2014, **14**, 4785–4791.
14 M. L. Tsai, S. H. Su, J. K. Chang, D. S. Tsai, C. H. Chen, C. I. Wu, L. J. Li, L. J. Chen and J. H. He, Monolayer MoS_2 heterojunction solar cells, *ACS Nano*, 2014, **8**, 8317–8322.
15 X. Li, W. Chen, S. Zhang, Z. Wu, P. Wang, Z. Xu, H. Chen, W. Yin, H. Zhong and S. Lin, 18.5% efficient graphene/GaAs van der Waals heterostructure solar cell, *Nano Energy*, 2015, **16**, 310–319.
16 D. J. Xue, S. C. Liu, C. M. Dai, S. Chen, C. He, L. Zhao, J. S. Hu and L. J. Wan, GeSe thin-film solar cells fabricated by self-regulated rapid thermal sublimation, *J. Am. Chem. Soc.*, 2017, **139**, 958–965.
17 M. Sun and U. Schwingenschlögl, δ-CS: A direct-band-gap semiconductor combining auxeticity, ferroelasticity, and potential for high-efficiency solar cells, *Phys. Rev. Appl.*, 2020, **14**, 044015.
18 M. Bernardi, M. Palummo and J. C. Grossman, Semiconducting monolayer materials as a tunable platform for excitonic solar cells, *ACS Nano*, 2012, **6**, 10082–10089.
19 M. Chhetri, S. Maitra, H. Chakraborty, U. V. Waghmare and C. N. R. Rao, Superior performance of borocarbonitrides, $B_xC_yN_z$, as stable, low-cost metal-free electrocatalysts for the hydrogen evolution reaction, *Energy Environ. Sci.*, 2016, **9**, 95–101.
20 J. Wang, J. Hao, D. Liu, S. Qin, D. Portehault, Y. Li, Y. Chen and W. Lei, Porous boron carbon nitride nanosheets as efficient metal-free catalysts for the oxygen reduction reaction in both alkaline and acidic solutions, *ACS Energy Lett.*, 2017, **2**, 306–312.
21 L. Cheng, J. Meng, X. Pan, Y. Lu, X. Zhang, M. Gao, Z. Yin, D. Wang, Y. Wang, J. You, J. Zhang and E. Xie, Two-dimensional hexagonal boron-carbon-nitrogen atomic layers, *Nanoscale*, 2019, **11**, 10454–10462.
22 W. Zhang, C. Chai, Q. Fan, Y. Song and Y. Yang, PBCF-graphene: A 2D sp^2 hybridized honeycomb carbon allotrope with a direct band gap, *ChemNanoMat*, 2020, **6**, 139–147.
23 G. Kresse and D. Joubert, From ultrasoft pseudopotentials to the projector augmented-wave method, *Phys. Rev. B: Condens. Matter Mater. Phys.*, 1999, **59**, 1758–1775.
24 R. J. Hunt, B. Monserrat, V. Zólyomi and N. D. Drummond, Diffusion quantum Monte Carlo and GW study of the electronic properties of monolayer and bulk hexagonal boron nitride, *Phys. Rev. B: Condens. Matter Mater. Phys.*, 2020, **101**, 205115.
25 R. Shinde, S. S. R. K. C. Yamijala and B. M. Wong, Improved band gaps and structural properties from Wannier-Fermi-Löwdin self-interaction corrections for periodic systems, *J. Phys.: Condens. Matter*, 2021, **33**, 115501.
26 X. Gonze and J. P. Vigneron, Density-functional approach to nonlinear-response coefficients of solids, *Phys. Rev. B: Condens. Matter Mater. Phys.*, 1989, **39**, 13120–13128.
27 S. Nosé, A unified formulation of the constant temperature molecular dynamics methods, *J. Chem. Phys.*, 1984, **81**, 511–519.
28 X. Kan, Y. Ban, C. Wu, Q. Pan, H. Liu, J. Song, Z. Zuo, Z. Li and Y. Zhao, Interfacial synthesis of conjugated two-dimensional N-graphdiyne, *ACS Appl. Mater. Interfaces*, 2018, **10**, 53–58.
29 N. Wang, X. Li, Z. Tu, F. Zhao, J. He, Z. Guan, C. Huang, Y. Yi and Y. Li, Synthesis and electronic structure of boron-graphdiyne with an sp-hybridized carbon skeleton and its application in sodium storage, *Angew. Chem., Int. Ed.*, 2018, **130**, 4032–4037.
30 A. Thomas, A. Fischer, F. Goettmann, M. Antonietti, J.-O. Müller, R. Schlögl and J. M. Carlsson, Graphitic carbon nitride materials: Variation of structure and morphology and their use as metal-free catalysts, *J. Mater. Chem. A*, 2008, **18**, 4893–4908.
31 F. Mouhat and F. X. Coudert, Necessary and sufficient elastic stability conditions in various crystal systems, *Phys. Rev. B: Condens. Matter Mater. Phys.*, 2014, **90**, 224104.
32 E. Cadelano, P. L. Palla, S. Giordano and L. Colombo, Elastic properties of hydrogenated graphene, *Phys. Rev. B: Condens. Matter Mater. Phys.*, 2010, **82**, 235414.
33 K. Liu, Q. Yan, M. Chen, W. Fan, Y. Sun, J. Suh, D. Fu, S. Lee, J. Zhou, S. Tongay, J. Ji, J. B. Neaton and J. Wu, Elastic properties of chemical-vapor-deposited monolayer MoS_2, WS_2, and their bilayer heterostructures, *Nano Lett.*, 2014, **14**, 5097–5103.
34 Q. Wei and X. Peng, Superior mechanical flexibility of phosphorene and few-layer black phosphorus, *Appl. Phys. Lett.*, 2014, **104**, 251915.
35 Y. Cai, G. Zhang and Y. W. Zhang, Polarity-reversed robust carrier mobility in monolayer MoS_2 nanoribbons, *J. Am. Chem. Soc.*, 2014, **136**, 6269–6275.
36 J. Qiao, X. Kong, Z.-X. Hu, F. Yang and W. Ji, High-mobility transport anisotropy and linear dichroism in few-layer black phosphorus, *Nat. Commun.*, 2014, **5**, 4475.

37 J. Du and J. Shi, 2D $Ca_3Sn_2S_7$ chalcogenide perovskite: A graphene-like semiconductor with direct bandgap 0.5 eV and ultrahigh carrier mobility 6.7×10^4 cm^2 V^{-1} s^{-1}, *Adv. Mater.*, 2019, **31**, 1905643.

38 V. Chakrapani, J. C. Angus, A. B. Anderson, S. D. Wolter, B. R. Stoner and G. U. Sumanasekera, Charge transfer equilibria between diamond and an aqueous oxygen electrochemical redox couple, *Science*, 2007, **318**, 1424–1430.

39 R. Nechache, C. Harnagea, A. Ruediger, F. Rosei and A. Pignolet, Effect of epitaxial strain on the structural and ferroelectric properties of Bi_2FeCrO_6 thin films, *Funct. Mater. Lett.*, 2010, **3**, 83–88.

40 S. Wang, M. S. Ukhtary and R. Saito, Strain effect on circularly polarized electroluminescence in transition metal dichalcogenides, *Phys. Rev. Res.*, 2020, **2**, 033340.

41 L. Du, C. Ren, L. Cui, W. Lu, H. Tian and S. Wang, Robust valley filter induced by quantum constructive interference in graphene with line defect and strain, *Phys. Scr.*, 2022, **97**, 125825.

42 M. Rohlfing and S. G. Louie, Electron–hole excitations in semiconductors and insulators, *Phys. Rev. Lett.*, 1998, **81**, 2312–2315.

43 G. Onida, L. Reining and A. Rubio, Electronic excitations: Density-functional *versus* many-body Green's-function approaches, *Rev. Mod. Phys.*, 2002, **74**, 601–659.

44 J. Liu, Y. Shen, X. Gao, L. Lv, Y. Ma, S. Wu, X. Wang and Z. Zhou, GeN_3 monolayer: A promising 2D high-efficiency photo-hydrolytic catalyst with High carrier mobility transport anisotropy, *Appl. Catal., B*, 2020, **279**, 119368.

45 T. Georgiou, R. Jalil, B. D. Belle, L. Britnell, R. V. Gorbachev, S. V. Morozov, Y. J. Kim, A. Gholinia, S. J. Haigh, O. Makarovsky, L. Eaves, L. A. Ponomarenko, A. K. Geim, K. S. Novoselov and A. Mishchenko, Vertical field-effect transistor based on graphene-WS_2 heterostructures for flexible and transparent electronics, *Nat. Nanotechnol.*, 2013, **8**, 100–103.

46 M. Palummo, M. Bernardi and J. C. Grossman, Exciton radiative lifetimes in two-dimensional transition metal dichalcogenides, *Nano Lett.*, 2015, **15**, 2794–2800.

47 S. Memaran, N. R. Pradhan, Z. Lu, D. Rhodes, J. Ludwig, Q. Zhou, O. Ogunsolu, P. M. Ajayan, D. Smirnov, A. Fernandez, F. J. García-Vidal and L. Balicas, Pronounced photovoltaic response from multilayered transition-metal dichalcogenides pn-junctions, *Nano Lett.*, 2015, **15**, 7532–7538.

